

Architectures of planetary systems formed by pebble accretion

Ryuji Morishima^{a,b,*}

^a*University of California, Los Angeles, Department of Earth, Planetary, and Space Sciences, Los Angeles, CA 90095, USA*

^b*Jet Propulsion Laboratory/California Institute of Technology, Pasadena, CA 91109, USA*

Abstract

In models of planetary accretion, pebbles form by dust coagulation and rapidly migrate toward the central star. Planetesimals may continuously form from pebbles over the age of the protoplanetary disk by yet uncertain mechanisms. Meanwhile, large planetary embryos grow efficiently by accumulation of leftover pebbles that are not incorporated in planetesimals. Although this process, called pebble accretion, is offering a new promising pathway for formation of giant planets' cores, architectures of planetary systems formed through the process remain elusive. In the present paper, we perform simulations of formation of planetary systems using a particle-based hybrid code, to which we implement most of the key physical effects as precisely as possible. We vary the size of a protoplanetary disk, the turbulent viscosity, the pebble size, the planetesimal formation efficiency, and the initial mass distribution of planetesimals. Our simulations show that planetesimals first grow by mutual collisions if their initial size is the order of 100 km or less. Once planetesimals reach ~ 1000 km in size, they efficiently grow by pebble accretion. If pebble supply from the outer region continues for a long period of time in a large protoplanetary disk, planetary embryos become massive enough to commence runaway gas accretion, resulting in gas giant planets. Our simulations suggest that planetary systems like ours form from protoplanetary disks with moderately high turbulent viscosities. If the disk turbulent viscosity is low enough, a planet opens up a gap in the gas disk and halts accretion of pebbles even before the onset of runaway gas accretion. Such a disk produces a planetary system with several Neptune-size planets.

Keywords: Accretion; Planetary formation; Origin, Solar System; Giant planets

1. Introduction

In a classic picture of planetary accretion, it has been generally assumed that all dust particles are instantaneously transformed into gravitationally-bound km-size planetesimals and that planets primarily grow by accumulation of planetesimals. Numerical simulations

*Corresponding author

Email address: morch116@gmail.com (Ryuji Morishima)

of planetary growth starting with only planetesimals (Inaba et al., 2003; Kobayashi et al., 2011; Chambers, 2014) showed that formation of giant planets’ cores of $\sim 10M_{\oplus}$ generally requires surface densities of planetesimals 5-10 times larger than that for the Minimum Mass Solar Nebula (MMSN; Hayashi, 1981).

The picture of planetary accretion has been dramatically changed recently. In a modern picture, pebbles first form by dust coagulation and then start rapid radial migration toward the central star (Birnstiel et al., 2010). Planetesimals may continuously form from migrating pebbles over the age of the protoplanetary disk by some yet uncertain mechanisms (Chambers, 2016). If a considerable amount of mass remains in pebbles, large planetary embryos grow efficiently by accumulation of pebbles, a process so called pebble accretion (Ormel and Klahr, 2010; Lambrechts and Johansen, 2012; Ida et al., 2016). If a planetary embryo grows massive enough, it starts rapid growth by accreting surrounding nebular gas, resulting in a gas giant planet (Pollack et al., 1996; Ikoma et al., 2000). Pebble accretion is offering a new promising pathway for formation of giant planets’ cores (Lambrechts and Johansen, 2014a; Bitsch et al., 2015; Levison et al., 2015; Chambers, 2016; Matsumura et al., 2017).

Chambers (2016) studied pebble accretion in viscously evolving disks and showed that formation of gas giant planets is efficient in gaseous disks with large initial sizes and low turbulent viscosities. Among studies of pebble accretion, only Chambers (2016) assumed continuous planetesimal formation from pebbles and varied initial planetesimal sizes while all other studies placed 1000 km-size or larger planetary embryos in the first place. These 1000 km-size planetary embryos are large enough for efficient growth due to pebble accretion. If initial planetesimals are not large enough, they primarily grow up by mutual merging. For formation of gas giant planets, small planetesimals need to grow up to ~ 1000 km in size before pebble supply from the outer part of the protoplanetary disk ceases (Chambers, 2016).

In the present study, we also study pebble accretion assuming continuous planetesimal formation from pebbles. Unlike Chambers (2016), we adopt a simple gas disk model in which the surface density is inversely proportional to the distance from the central star and decays exponentially with time, rather than solving viscous diffusion. Viscous spreading probably occurs during the early stage of disk evolution, while this mechanism is generally too slow to explain observed gas dissipation timescales (see Stepinski, 1998; Chambers, 2009). This implies that some non-viscous mechanisms, such as photoevaporation (Owen et al., 2012) or magnetocentrifugal winds (Bai, 2013; Suzuki and Inutsuka, 2014), predominantly work during middle to late stage of disk evolution. Therefore, we give the evolution of gas surface density independent from the turbulent viscosity, assuming that planet formation proceeds mostly in the middle to late stage of disk evolution. This assumption will make the dependence of final masses of gas giant planets on the turbulent viscosity different from that was found by Chambers (2016).

The numerical method we employ is the particle-based hybrid code for planet formation developed by Morishima (2015). This Lagrangian type code can handle detailed orbital dynamics of any solid bodies, since it numerically integrates orbits of all types of solid bodies. The code can accurately handle spatial non-uniformity of planetesimals and pebbles, mean

motion resonances, and planetesimal-driven migration. However, Lagrangian simulations are computationally intense and we need to limit a simulation domain to outside the snow line (~ 3 AU) in order to simulate planetary formation processes over the lifetime of a protoplanetary disk, $\sim 3\text{--}5$ Myr. Our method is similar to the one employed by Levison et al. (2015), who adopted disks with a compact size (30 AU) and high surface densities. Unlike their simulations, we employ disks with large sizes (100-200 AU) and moderately low surface densities, as large disks are favorable for formation of giant planets (Chambers, 2016). We also vary the initial planetesimal size and the turbulent viscosity whereas those were fixed in Levison et al. (2015).

The present paper is organized as follows. Section 2 describes modifications made to our particle-based hybrid code for handling pebble accretion. In Section 3, we introduce our disk model and explain all effects taken into account in our simulations. Section 4 shows some simulation examples. In Section 5, we discuss the parameter dependence of architectures of planetary systems. Future work will be discussed in Section 6. Section 7 summarizes main findings.

2. Simulation codes

2.1. Code overview

We use a particle-based hybrid code developed by Morishima (2015). The code has four classes of particles: full-embryos, sub-embryos, planetesimal-tracers, and pebble-tracers. Pebble-tracers are newly added for the present study and we will describe differences between planetesimal-tracers and pebble-tracers in detail below. Orbits of any types of particles are directly integrated. The accelerations due to planetary embryos' gravity are directly calculated by the N -body routine. The code can handle a large number of small planetesimals/pebbles using the super-particle approximation, in which a large number of small planetesimals/pebbles are represented by a small number of tracers.

As planetesimals grow, the number of planetesimals in a tracer decreases. Once the number of planetesimals in a tracer becomes unity and its mass exceeds the threshold mass M_{t0} , this particle is promoted to a sub-embryo. If the mass of the sub-embryo exceeds $100M_{t0}$, it is further promoted to a full-embryo. The acceleration of the sub-embryo due to gravitational interactions with surrounding planetesimals is handled by the statistical routine in order to avoid artificially strong accelerations on the sub-embryo while the acceleration of the full-embryo is always calculated by the N -body routine. The algorithms and various tests for the validation of the code are described in detail in Morishima (2015, 2017).

2.2. Pebble-tracers

We introduce pebble-tracers. We conventionally define a pebble-tracer as a tracer of small bodies with $St < 2$, where St is the Stokes number (Eq. (6)). A tracer of bodies with $St \geq 2$ is called as a planetesimal-tracer. The boundary value, $St = 2$, is based on the study of Ormel and Kobayashi (2012), who showed a change of modes of pebble accretion at $St = 2$ for a low relative velocity.

Gravitational and collisional interactions between planetesimal-tracers are handled in the statistical routine using the Keplerian elements of planetesimal-tracers, as described in Morishima (2015). This approach is inappropriate for pebbles which are strongly coupled with gas. The collisional probability of pebbles with a planetesimal is calculated by a new routine, where their relative velocities are used instead of their relative Keplerian elements (Section 3.3 and Appendix. C). The damping effect on planetesimals due to collisions with pebbles is also included in this routine. The gravitational and collisional interactions between pebbles and embryos are directly handled in the N -body routine. We ignore any gravitational and collisional interactions between pebble-tracers. We also ignore gravitational interactions (stirring and dynamical friction) between pebbles and planetesimals.

It is technically possible to handle collisional interactions between pebble-tracers, although simulations in the present paper do not generally have sufficient numbers of pebble-tracers to derive accurate mutual collisional rates and resulting size distributions of pebbles. Instead of directly handling mutual collisions, we adopt two cases for evolution of sizes of pebbles during their radial migration. The first one adopts a constant St number (except the pebble size is fixed during close encounters with embryos). This resembles the outcome of simulations of dust coagulation without any collisional destruction (Birnstiel et al., 2012; Sato et al., 2016). These simulations show that St for the largest pebbles remains around 0.1-1. The another case adopts a constant pebble size. This makes St decrease as pebbles migrate inward. This approximation roughly mimics prevention of growth of pebbles due to destructive collisions (Birnstiel et al., 2012; Chambers, 2016). We do not consider porosity change of pebbles, although some studies indicate its importance (Okuzumi et al., 2012; Krijt et al., 2015).

2.3. Collisions of tracers with sub-embryos

In our previous studies (Morishima, 2015, 2017), collisions of tracers with sub-embryos were handled in the statistical routine, where we did not let a tracer and a sub-embryo merge in the N -body routine even if they mutually overlap. This treatment is found to be problematic if tracers with small constituent bodies encounter with sub-embryos in a gaseous disk. Small bodies are often gravitationally captured by sub-embryos and need to be merged with sub-embryos in the N -body routine. To avoid duplicative counting both in the statistical and N -body routines, we handle collisions between tracers and sub-embryos only in the N -body routine in the present study.

This approach has two drawbacks. First, after a tracer is promoted to a sub-embryo, a first impact in the N -body routine roughly doubles the mass of the sub-embryo. This effect makes an artificial kink around M_{t0} in the mass distribution, as discussed in Levison et al. (2012). This effect is, however, not essential as far as we focus on planets that are much more massive than M_{t0} . Second, the collisional damping effect on a sub-embryo is not correctly handled. In the N -body routine, a tracer fully feels the gravitational force of a sub-embryo while the sub-embryo feels only the gravitational force of a single constituent planetesimal in the tracer. During a close encounter between them, the tracer is highly accelerated while the sub-embryo has only a slight velocity change. If we add the entire momentum of a tracer

to the sub-embryo after they merge, it causes an artificially large acceleration of the sub-embryo. To avoid this effect, we only add the momentum a constituent planetesimal/pebble to that of the sub-embryo. This treatment unfortunately underestimates the collisional damping effect, although dynamical friction due to surrounding planetesimals, handled in the statistical routine, is generally much more important.

3. Simulation setup

3.1. Effects of gas on orbital evolution

We first describe gaseous forces acting on particles over a wide size range. Through the paper, we use the cylindrical coordinates (r, θ, z) . We assume that the gas surface density Σ_{gas} varies as a function of distance r and time t as

$$\Sigma_{\text{gas}}(r, t) = 500 \left(\frac{r}{1 \text{ AU}} \right)^{-1} \exp \left(-\frac{t}{\tau_{\text{gas}}} \right) \text{ g cm}^{-2}, \quad (\text{for } r \leq r_{\text{disk}}) \quad (1)$$

where r_{disk} is the disk size and τ_{gas} is the gas dissipation timescale. We adopt the most typical value $\tau_{\text{gas}} = 1 \text{ Myr}$ suggested from observations of protoplanetary disks around nearby solar-type protostars (Ohsawa et al., 2015).

The temperature profile is given as (Hayashi, 1981)

$$T = 280 \left(\frac{r}{1 \text{ AU}} \right)^{-1/2} \text{ K}. \quad (2)$$

The disk viscosity ν is given by the α model (Shakura and Sunyaev, 1973) as

$$\nu = \alpha c h_{\text{gas}}, \quad (3)$$

where c is the isothermal sound velocity and $h_{\text{gas}} = c/\Omega$ is the gaseous scale height, $\Omega = (GM_*/r^3)^{1/2}$ is the Keplerian frequency, G is the gravity constant, and M_* is the mass of the central star, which we assume to be the solar mass M_{\odot} . We adopt the molecular weight of 2.33. This gives $c = 1.0 \times 10^5 (r/1 \text{ AU})^{-1/4} \text{ cm s}^{-1}$. The combination of the radial profiles of Σ_{gas} (Eq. (1)) and T (Eq. (2)) gives a steady state (radially constant) mass accretion rate of the global disk toward the central star as

$$\dot{M}_{\text{glob}} = 3\pi \Sigma_{\text{gas}} \nu = 3.7 \times 10^{-9} \left(\frac{\alpha}{10^{-3}} \right) \exp \left(-\frac{t}{\tau_{\text{gas}}} \right) M_{\odot} \text{ yr}^{-1}. \quad (4)$$

The velocity vectors of a solid body and gas are given by \mathbf{v} and \mathbf{v}_{gas} , respectively. Their relative velocity is defined as $\mathbf{v}_{\text{rel}} = \mathbf{v} - \mathbf{v}_{\text{gas}}$. The aerodynamic drag force per unit mass is given by (Adachi et al., 1976)

$$\mathbf{f}_{\text{drag}} = -\frac{1}{2M} C_D \pi s^2 \rho_{\text{gas}} v_{\text{rel}} \mathbf{v}_{\text{rel}} = -\frac{\Omega}{\text{St}} \mathbf{v}_{\text{rel}}, \quad (5)$$

where C_D is a numerical coefficient (Appendix A), M and s are the mass and the radius of the body, ρ_{gas} is the gas density, $v_{\text{rel}} = |\mathbf{v}_{\text{rel}}|$, and St is the Stokes number of the body. For a small body in the Epstein drag regime, C_D and St are given as

$$C_{D,\text{Eps}} = \frac{8c_m}{3v_{\text{rel}}}, \quad \text{St}_{\text{Eps}} = \frac{\rho_p s \Omega}{\rho_{\text{gas}} c_m}, \quad (6)$$

where $c_m = (8/\pi)^{1/2}c$ is the thermal velocity and ρ_p is the material density of the solid body.

The gas velocity is given by a sum of the laminar component $\mathbf{v}_{\text{lam}} = (0, v_{\text{lam},\theta}, 0)$ and the turbulent component $\mathbf{v}_{\text{tur}} = (v_{\text{tur},r}, v_{\text{tur},\theta}, v_{\text{tur},z})$ as

$$\mathbf{v}_{\text{gas}} = \mathbf{v}_{\text{lam}} + \mathbf{v}_{\text{tur}}, \quad (7)$$

The laminar component $v_{\text{lam},\theta}$ in the θ direction is obtained by the force balance in the r direction (Morishima et al., 2010). We give the turbulent component using a Lagrangian stochastic model (Wilson and Sawford, 1996). This model approximately handles the largest turbulent eddies while smaller eddies are ignored. We assume that turbulence is isotropic, that three velocity components are uncoupled, and that the turnover timescale of eddies is Ω^{-1} . The change of $v_{\text{tur},r}$ of gas around each body during the time step δt is given as

$$\delta v_{\text{tur},r} = -v_{\text{tur},r} \Omega \delta t + \sigma_{\text{tur}} \xi \sqrt{2\Omega \delta t}, \quad (8)$$

where $\sigma_{\text{tur}} = (\alpha/3)^{1/2}c$ is the standard deviation of each velocity component (the factor of 3 comes from the three velocity components) and ξ is the Gaussian white noise, which has the standard deviation of unity ($\langle \xi^2 \rangle = 1$) and is uncorrelated in time and space. The other velocity components, $v_{\text{tur},\theta}$ and $v_{\text{tur},z}$ are given in a similar fashion. This simple approach correctly reproduces the scale height of pebbles (Fig. 1). Since \mathbf{v}_{tur} is calculated for each particle independently, this model does not give correct collision velocities between small pebbles ($\text{St} \ll 1$) that are tightly coupled with turbulent motion (see Ormel and Cuzzi, 2007). This is not a problem as we do not explicitly handle collisions between pebbles (Section 2.2).

While pebbles are mainly stirred by the aerodynamic coupling with turbulent motion, planetesimals and larger bodies are more affected by gravitational interactions with gas density fluctuations (Laughlin et al., 2004; Ida et al., 2008; Okuzumi and Ormel, 2013). We ignore this effect except for one run (Run 16) where we adopt the recipe of Okuzumi and Ormel (2013) (Appendix B).

Orbital eccentricities and inclinations of massive bodies are damped by tidal interactions with the gaseous disk (Papaloizou and Larwood, 2000; Tanaka and Ward, 2004; Capobianco et al., 2011). We use the formula of Papaloizou and Larwood (2000) for the tidal damping effects. In the present paper, we ignore Type I and Type II migration due to tidal interactions with the gaseous disk. We also ignore the gravitational potential of the global gaseous disk.

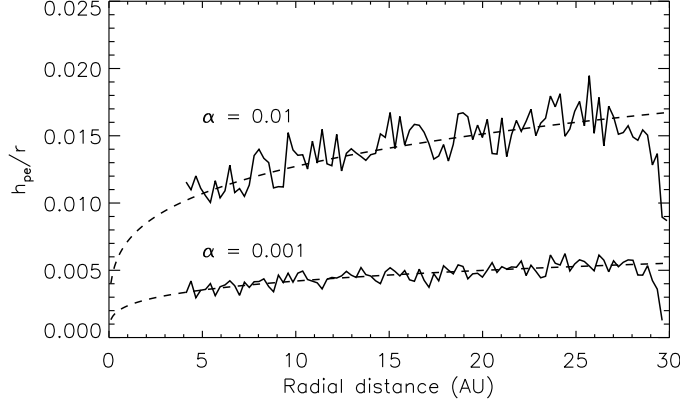


Figure 1: Vertical scale height of pebble-tracers for $\text{St} = 0.1$ and $\alpha = 0.01$ and 0.001 . Pebble-tracers are released at $r = 30$ AU and deleted at $r = 4$ AU. The solid curves are the scale heights from simulations, $h_{\text{pe}} = \langle z^2 \rangle^{1/2}$. Hundreds of snapshots are superposed to reduce statistical noises. The dashed curves are the theoretical predictions, $h_{\text{pe}} = (1 + \gamma)^{-1/4} \sqrt{\alpha/(\alpha + \text{St})} h_{\text{gas}}$ (Dubrulle et al., 1995), where γ is the power-law for the eddy energy spectrum. Our simulations show good agreements with theoretical predictions for $\gamma = 3$.

3.2. Formation of pebbles and planetesimals

We adopt a simple, analytic model for pebble formation. We assume all the solid component in the protoplanetary disk is all in tiny (μm -size) dust grains at $t = 0$. The dust surface density at $t = 0$ is assumed as

$$\Sigma_{\text{dust}}(r, t = 0) = Z_0 \Sigma_{\text{gas}}(r, t = 0), \quad (9)$$

where Z_0 is the metallicity $Z = \Sigma_{\text{dust}}/\Sigma_{\text{gas}}$ at $t = 0$ and we adopt the solar metallicity of 0.014 (Lodders, 2010) in the present paper.

We assume that tiny dust particles do not radially move but grow by mutual sticking. The growth timescale during which μm -size dust grains grow to mm-size pebbles is (Lambrechts and Johansen, 2014a)

$$\tau_{\text{peb}}(r, Z) = \frac{4 \log(s_{\text{peb}}/s_{\text{dust}})}{\sqrt{3} \epsilon_{g,d} Z} \Omega^{-1}, \quad (10)$$

where s_{peb} and s_{dust} are the radii of dust and pebble particles, $\epsilon_{g,d}$ is the sticking probability for dust-dust collisions. We set $\log(s_{\text{peb}}/s_{\text{dust}}) = 10$ and $\epsilon_{g,d} = 0.1$. This small value of $\epsilon_{g,d}$ gives the dust life time consistent with observations while dust depletion is too rapid for $\epsilon_{g,d} = 1$. The dust abundance is assumed to decay on a timescale of τ_{peb} due to production of pebbles as

$$\frac{d\Sigma_{\text{peb}}}{dt} = -\frac{d\Sigma_{\text{dust}}}{dt} = \frac{\Sigma_{\text{dust}}}{\tau_{\text{peb}}}, \quad (11)$$

where Σ_{peb} is the pebble surface density. Using Eqs. (1) and (9)–(11), the dust surface density at r as a function of time t is derived as

$$\frac{\Sigma_{\text{dust}}(t)}{\Sigma_{\text{dust}}(t=0)} = \left[\frac{\tau_{\text{gas}}}{\tau_{\text{peb}}(r, Z_0)} \left(\exp\left(\frac{t}{\tau_{\text{gas}}}\right) - 1 \right) + 1 \right]^{-1}. \quad (12)$$

The growth timescale of dust particles is long at large distance while it is shortened by gas depletion as $\tau_{\text{peb}} \propto Z^{-1}$. For $t \ll \tau_{\text{gas}}$, $\Sigma_{\text{dust}}(t) \propto (t/\tau_{\text{peb}}(r, Z_0) + 1)^{-1}$ while for $t \gg \tau_{\text{gas}}$, $\Sigma_{\text{dust}}(t) \propto \exp(-t/\tau_{\text{gas}})$ as is the case of gas.

To handle production of pebble-tracers, we make radial grids. If the total mass of pebbles produced in a grid cell during a time interval exceeds the tracer mass M_{t0} , we make a new pebble-tracer at r with a constituent pebble size determined from the assigned St (Eq. (6)). The time interval is measured from the time at which the previous pebble-tracer was produced at the same location r to the present time. Once pebbles form, they start migrating inward due to gas drag. In the present study, pebble-tracers are either (1) converted into planetesimals, (2) merged with existing planetesimals or embryos, or (3) removed at the snow line r_{snow} . To save the computational time, we perform orbital integration of pebble-tracers only in the region inside the cut-off radius r_{cut} ($r_{\text{snow}} < r_{\text{cut}} < r_{\text{disk}}$). If a pebble-tracer forms at a certain location r beyond r_{cut} at time t , we introduce it to the simulation at r_{cut} and at $t + \delta t$, where δt is a time for the pebble-tracer to migrate from r to r_{cut} . If this pebble-tracer is converted into a planetesimal-tracer before reaching r_{cut} , we delete it.

Given large uncertainties in planetesimal formation mechanisms, efficiencies, and locations, we employ a parameterized approach. Pebbles are converted into planetesimals on the timescale τ_{plan} as (Chambers, 2016)

$$\frac{d\Sigma_{\text{plan}}}{dt} = \frac{\Sigma_{\text{peb}}}{\tau_{\text{plan}}}. \quad (13)$$

In our simulations, this simply means that a pebble-tracer is converted into a planetesimal-tracer on the average timescale of τ_{plan} . We adopt a following form for τ_{plan} :

$$\tau_{\text{plan}} = \tau_{\text{plan1}} \frac{1 + \text{St}^2}{2\text{St}} \frac{\Omega(1 \text{ AU})}{\Omega(r)}, \quad (14)$$

where τ_{plan1} is the planetesimal formation timescale from pebbles with $\text{St} = 1$ at $r = 1 \text{ AU}$. The radial velocity of a pebble is given as

$$v_r = \frac{1 + \text{St}^2}{2\text{St}} \eta r \Omega, \quad (15)$$

where η is the fractional deviation of gas velocity relative to the Keplerian velocity. With the correction factor $(1 + \text{St}^2)/(2\text{St})$ in Eq. (14), $d\Sigma_{\text{plan}}/dt$ becomes independent of St as $\Sigma_{\text{peb}} \propto v_r^{-1}$.

We assume the following initial mass-frequency distribution of planetesimals:

$$\frac{dM}{dN} \propto M^{-1.6} \quad (\text{for } 10^{-3}M_0 \leq M \leq M_0), \quad (16)$$

where dN is the number of bodies between M and $M + dM$, the power-law exponent -1.6 from simulations of streaming instability is adopted (Johansen et al., 2015; Carrera et al., 2015; Simon et al., 2016; Schäfer et al., 2017). The default value for the largest initial planetesimal is $M_0 = 10^{21}$ g. This case can reproduce a bump around 10^{21} g seen in the mass-frequency distributions of asteroids and Kuiper belt objects (Morbidelli et al., 2009; Johansen et al., 2015). However, we also vary M_0 , since the initial size of planetesimals is still a matter of debate (e.g. Weidenschilling, 2011). The initial velocity dispersion of planetesimals is assumed to be 0.1 times of the escape velocity of the largest initial planetesimal. The initial semimajor axis of the planetesimal-tracer is chosen so that the its z -component of the orbital angular momentum is the same as its progenitorial pebble-tracer.

3.3. Collision rate and outcome

The collision probability between planetesimals ($St \geq 2$) in two different planetesimal-tracers is given by the recipe of Morishima (2015). Ormel and Klahr (2010) showed that even for impactors with $St > 2$, the collision probability is significantly enhanced due to three body capture, if the relative velocity is low enough. We take into account this effect using the prescription for the three body regime given by Ormel and Kobayashi (2012) (Appendix C). Ormel and Klahr (2010) also showed that if pebbles ($St < 2$) encounter with an embryo at low relative velocities, they settle toward the embryo at the terminal velocities (the settling regime). If the relative velocities of pebbles are large, the gas drag during encounters with the embryo can be ignored (the hyperbolic regime). We adopt the collision probabilities of pebbles with planetesimals/embryos in the settling and hyperbolic regimes again given by Ormel and Kobayashi (2012) (Appendix C).

For planetesimal-planetesimal collisions or pebble-planetesimal collisions, we take into account collisional destruction (Benz and Asphaug, 1999; Kobayashi and Tanaka, 2010). The detailed prescription is described in Appendix D. The smallest size of collisional fragments is assumed to be the same as the pebble size at each location.

As described in Sections 2, collisions of tracers with full- and sub-embryos are directly handled in the N -body routine. The routine can automatically reproduce the pebble accretion rate of embryos without using any analytic recipes. If a tracer hits an embryo, the outcome is either merging or rebound. We adopt the boundary velocity for these two outcomes given by Genda et al. (2012). If a tracer is gravitationally captured by an embryo during their close encounter, we merge them without integrating their orbits until the impact. We judge a pair of bodies are gravitationally bound if the mutual distance is less than 0.1 Hill radius and the Jacobi integral in Hill units is less than -3.0 (see Nakazawa et al., 1989, for the integral). We confirmed that these criteria are conservative enough in test simulations.

The collisional radius of an embryo is enhanced due to its dense atmosphere (Inaba and Ikoma, 2003; Ormel and Kobayashi, 2012). The enhanced collisional radius (Appendix E) is used

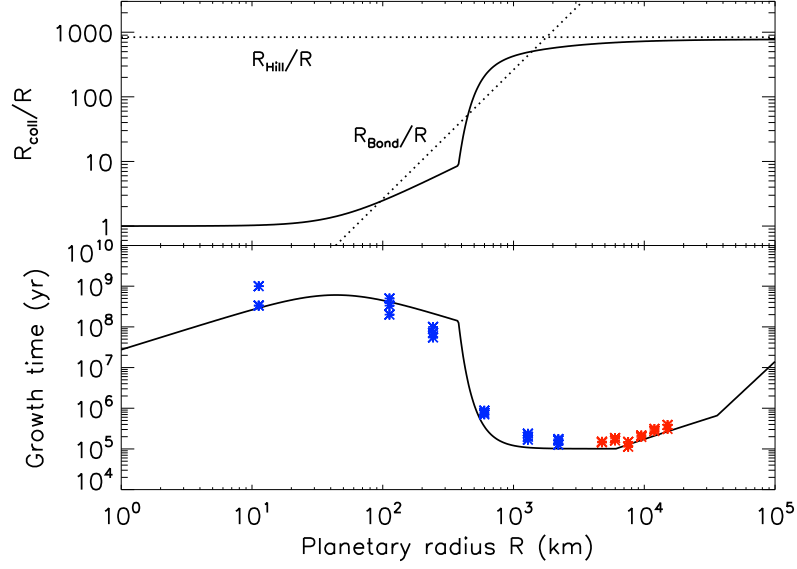


Figure 2: Top: Collisional radius R_{coll} for pebble accretion (Ormel and Kobayashi, 2012) relative to the geometric radius R at 5 AU for $\text{St} = 0.1$ and $\alpha = 10^{-3}$. The target body is assumed to have a circular and non-inclined orbit. The Hill radius, R_{Hill} , and the Bondi radius for pebble accretion, $R_{\text{Bond}} = GM/v_{\text{hw}}^2$, are shown by dashed lines, where $v_{\text{hw}} (= 46 \text{ m/s})$ is the headwind velocity. Bottom: The growth time scale M/\dot{M} of an embryo for the pebble mass flux of $100M_{\oplus} \text{ Myr}^{-1}$. The solid line is the theoretical expectation (Ormel and Kobayashi, 2012). The asterisks are those from our simulations; the blue asterisks are from the statistical routine while the red asterisks are from the N -body routine. The kink at $R \sim 400 \text{ km}$ is the transition from the hyperbolic regime to the settling regime. The kink at $R \sim 5000 \text{ km}$ is the transition from 3D to 2D accretion ($R_{\text{coll}} = h_{\text{pe}}$). The kink at $R \sim 40000 \text{ km}$ is caused by a fact that a larger embryo sweeps up all pebbles crossing the embryo's orbit ($\dot{M} = \text{const}$).

instead of the radius of the solid core. The enhanced collisional radius primarily depends on the atmospheric opacity κ and the mass accretion rate of the embryo \dot{M} . We adopt $\kappa = 0.1 \text{ cm}^2/\text{g}$. The accretion rate \dot{M} is derived from the collision log of the embryo. We search an impact at which the mass of the embryo is closest to 90% of the present mass. Using the time t_{90} and the mass M_{90} of the embryo at this impact, we approximately give the mass accretion rate as

$$\frac{dM}{dt} = \frac{M - (M_{90} + 0.5\delta M)}{t - t_{90}}, \quad (17)$$

where δM is the mass gain by the impact. This mass accretion rate is also used for judging the onset of runaway gas accretion to the embryo (Section 3.4).

Figure 2 shows the collisional radius and the growth timescale of a target body for pebble accretion ($\text{St} = 0.1$). The collisional radius is almost similar to the geometric radius for small planetesimals while it significantly increases with radius in the radius range of 100 km to 1000 km. The growth timescales of target bodies in our test simulations show good agreements with the theoretical predictions for all the range of the target radius.

3.4. Runaway gas accretion and gap opening

If the embryo's mass exceeds the critical mass, it starts runaway gas accretion from the global gas disk. The critical mass is given by (Ikoma et al., 2000) as

$$M_{\text{crit}} = 7 \left(\frac{\dot{M}}{1 \times 10^{-7} M_{\oplus} \text{ yr}^{-1}} \right)^{0.25} \left(\frac{\kappa}{1 \text{ cm}^2 \text{ g}^{-1}} \right)^{0.25} M_{\oplus}, \quad (18)$$

where κ is the atmospheric opacity. We ignore the atmospheric mass until the embryo starts runaway gas accretion for simplicity, although accurate atmosphere models (Pollack et al., 1996; Ikoma et al., 2000) show that the atmospheric mass is comparable to the core mass at the onset of runaway gas accretion.

When the embryo mass is relatively small, the gas accretion rate for the embryo is regulated by the cooling efficiency of its atmosphere:

$$\dot{M}_{\text{KH}} = \frac{M}{\tau_{\text{KH}}}, \quad (19)$$

where τ_{KH} is the Kelvin-Helmholz (cooling) time given as (Ikoma et al., 2000)

$$\tau_{\text{KH}} = 10^8 \left(\frac{M_{\text{core}}}{M_{\oplus}} \right)^{-2.5} \left(\frac{\kappa}{1 \text{ cm}^2 \text{ g}^{-1}} \right) \text{ yr}. \quad (20)$$

When an embryo becomes massive enough, the gas accretion rate for the embryo is regulated by the global accretion rate \dot{M}_{glob} (Eq. (4)). Numerical simulations of Lubow and D'Angelo (2006) showed that the growth rate of a gas capturing embryo is about 75–90 % of the global disk accretion rate outside its orbit. We adopt 90% for this ratio and therefore give the gas accretion rate as

$$\dot{M} = \text{MIN}(\dot{M}_{\text{KH}}, 0.9\dot{M}_{\text{glob}}). \quad (21)$$

Accordingly, the global accretion rate inside the orbit of the gas capturing embryo is subtracted by \dot{M} . This correction is important since it is found to be common in our simulations that multiple embryos undergo runaway gas accretion in the same time.

A massive embryo opens up a gap around its orbit in the global gaseous disk (Lubow and D’Angelo, 2006; Duffell, 2015; Kanagawa et al., 2017). Based on angular momentum conservation, Duffell (2015) derived an analytic formula of the radial profile of a gaseous gap induced by an embedded embryo with the semimajor axis a as

$$\Sigma_{\text{gas}}(r, K) = \Sigma_{\text{gas}}(r, K = 0) \left(1 - \frac{0.048 f(r) K}{1 + 0.048 K} \sqrt{a/r} \right), \quad (22)$$

where

$$K = \left(\frac{M}{M_*} \right)^2 \left(\frac{h_{\text{gas}}}{a} \right)^{-5} \alpha^{-1}. \quad (23)$$

The function $f(r)$ is the non-dimensional angular momentum flux due to shocking of planetary wakes. The function $f(r)$ can be described in terms of the scaled distance $d(r)$ from the planet as

$$f(r) = \begin{cases} 1 & (\text{for } d(r) \leq d_{\text{sh}}), \\ \sqrt{d_{\text{sh}}/d(r)} & (\text{for } d(r) > d_{\text{sh}}), \end{cases} \quad (24)$$

where the scaled shock position d_{sh} was calculated by Goodman and Rafikov (2001) as

$$d_{\text{sh}} = 1.89 + 0.53 \left(\frac{M}{M_*} \right)^{-1} \left(\frac{h_{\text{gas}}}{a} \right)^3. \quad (25)$$

The scaled distance $d(r)$ is given as

$$d(r) = 0.93 \left(\frac{|r - a|}{h_{\text{gas}}} \right)^{5/2}. \quad (26)$$

The surface density profiles around orbits of embryos more massive than $2M_{\oplus}$ are modified using Eq. (22). If multiple embryos open gaps, we calculate the surface densities reduced by gap opening embryos individually and takes the lowest value at each radial location. Note also that Duffell (2015) ignored the effect of gas accretion to the embryo for derivation of Eq. (22). Thus, the surface density profile inside the orbit of a gas capturing embryo is not fully consistent with the global gas accretion rate in our model, although this effect is minor for overall growth of embryos.

If the embryo is more massive than a certain threshold mass, the rotation velocity of gas exceeds the local Keplerian velocity near the outer edge of the gap. The super Keplerian rotation prevents pebbles from inward migration and accretion to the embryo. Figure 3 shows the threshold mass, called the pebble isolation mass, numerically derived from Eq. (22). Lambrechts and Johansen (2014b) performed hydrodynamic simulations and showed that the pebble isolation mass is about $20M_{\oplus}$ for $\alpha = 6 \times 10^{-3}$ and at $a = 5$ AU. This is roughly consistent with the value in Fig. 3, $M \simeq 27M_{\oplus}$. The pebble isolation mass decreases with decreasing the viscosity. For example, it is about $12M_{\oplus}$ for $\alpha = 1 \times 10^{-3}$ at $a = 5$ AU. If the viscosity is further lower, embryos can reach the pebble isolation mass even before they start runaway gas accretion.

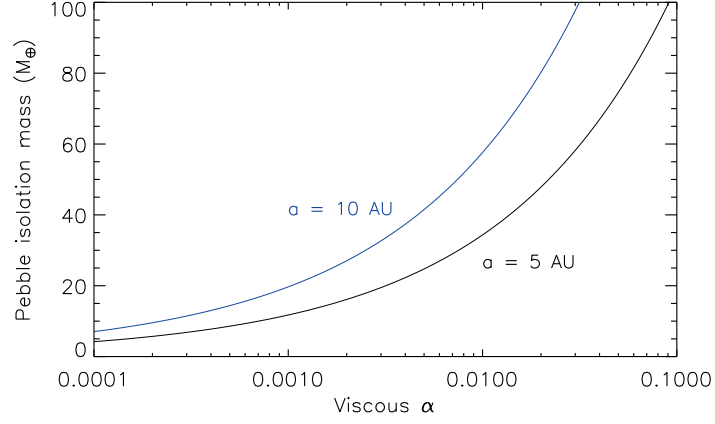


Figure 3: Pebble isolation mass. The analytic prescription of Duffell (2015) for gap radial profiles is adopted.

Run	α	St	M_0 (g)	τ_{plan1} (yr)	r_{disk} (AU)	r_{snow} (AU)	Turb. torque
1	3×10^{-3}	0.1	10^{21}	100	200	3	No
1b							
1c							
2	1×10^{-4}						
3	3×10^{-4}						
4	1×10^{-3}						
5	1×10^{-2}						
6			10^{13}				
7			10^{17}				
8			10^{25}				
9				1000			
10			10^{25}	1000			
11		0.03					
12		0.3					
13		$0.03(a/3 \text{ AU})$					
14					100		
15						4	
16							Yes

Table 1: Input parameters. The values at empty spaces are the same as those for Run 1. For Run 13, $\text{St} = 0.2$ for $a > r_{\text{cut}} = 20 \text{ AU}$.

4. Simulation runs

The input parameters for 18 simulations we performed are summarized in Table 1. Run 1 is a base line case and we vary one or two different parameters from the base-line case for other runs. For $\tau_{\text{plan1}} = 100$ yr, roughly a half of pebbles are converted into planetesimals before reaching the snow line r_{snow} , provided that they neither merge with existing planetesimals/embryos nor are trapped at the edges of planetary gaps. Planetesimals and pebbles are removed if their semimajor axes become less than r_{snow} . We do not remove embryos even inside the snow line, as they are likely to gravitationally retain atmospheres consisting of water vapor (Machida and Abe, 2010). We remove embryos if they are inside 2 AU. The time step of orbital integration is 7.5 days. The initial mass of a pebble-tracer at its introduction is $M_{t0} = 0.02M_{\oplus}$. This is also the minimum mass of a sub-embryo. We performed each run up to > 5 Myr. For Run 2, we exceptionally stopped the simulation before 4 Myr, as a chain of planets form beyond $r_{\text{cut}} (= 20 \text{ AU})$ by that time. Each run takes 2-3 CPU weeks. In the following, we first describe processes of planetary growth in detail for three distinctive cases: Runs 1, 2, and 10.

4.1. Run 1

We begin with the base-line case, Run 1. This is one of a few runs which produced a planetary system similar to our Solar System. The diameter of the initially largest planetesimal is about 100 km. The viscosity parameter is moderately high ($\alpha = 3 \times 10^{-3}$). The distributions of mass and orbital eccentricities at three different times are shown in the upper panel of Fig. 4. The time evolutions of masses and semimajor axes of massive embryos ($> 2M_{\oplus}$) are shown in the lower panel of Fig. 4.

Since planetesimals immediately after their formation are not large enough for efficient pebble accretion (see Fig. 2), they first grow by mutual collisions. Once the largest planetesimals reach ~ 1000 km in size ($M \sim 10^{24}$ g), they grow more efficiently by pebble accretion than by planetesimal accretion. The two most massive embryos reach $1M_{\oplus}$ in mass around 0.6 Myr near the snow line. They further grow and reach $10M_{\oplus}$ in mass around 2 Myr, at which they start runaway gas accretion. The outer embryo grows much more rapidly than the inner one, since the outer one reduces the global gas accretion rate inside its orbit. The mass of the largest embryo is about 1.3 and 1.5 times of the Jupiter’s mass at 3 and 5 Myr, respectively. The largest embryo opens up a gap in a gas disk and accretion of pebbles to the embryo no longer occurs (for $M > 60M_{\oplus}$; see Fig. 3). However, core growth of the largest embryo occurs even after the onset of runaway gas accretion since many planetesimals are scattered toward the largest embryo by outer embryos, which are not massive enough to efficiently eject planetesimals from the system.

During gas accretion of the inner two embryos, five massive embryos form outside the orbit of the most massive embryo. These outer embryos migrate outward, as they grow due to mutual orbital repulsion. Some of them also experience rapid planetesimal-driven migration. One of the outer embryos has a very large orbital eccentricity due to gravitational perturbations of other embryos and is ejected from the system at 4.6 Myr. Two of the outer embryos at ~ 11 and ~ 15 AU start runaway gas accretion around 4 Myr, and the outer one

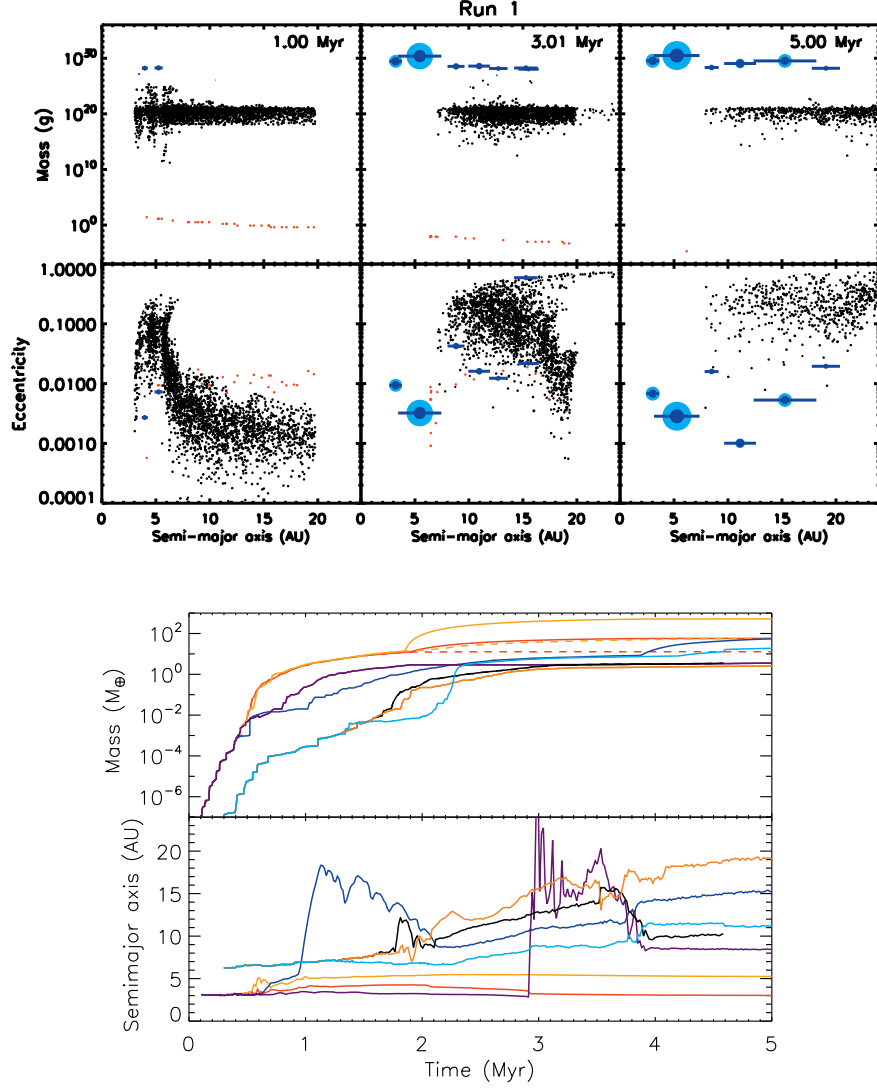


Figure 4: (Top) Distributions of mass and orbital eccentricity for Run 1 at three different times. Blue, black, and red circles show embryos, planetesimals, and pebbles. For embryos, the radius of each circle is proportional to the embryo’s radius. For gas capturing embryos, each atmosphere is shown by the light-blue annulus around the blue-coded core. A half length of a horizontal bar is 10 Hill radii for each embryo with a mass more than M_\oplus . Since the orbital eccentricity of each body is derived assuming a Keplerian orbit, pebble-tracers have apparent orbital eccentricities of $\sim \eta$. (Bottom) Time evolutions of masses and semimajor axes of most massive embryos. Two dotted curves show core masses of two gas capturing embryos.

reaches $\sim 60M_{\oplus}$ at 5 Myr. If the gaseous disk completely dissipates around 4 Myr, and if outer four embryos merge into two embryos, they may result in like Uranus and Neptune. At the end of simulation, the mass-frequency distribution of remaining planetesimals (mostly at > 10 AU) is almost the same as the original distribution.

4.2. Run 2

The input parameter for Run 2 are the same as those for Run 1 except that the viscosity parameter for Run 2 ($\alpha = 1 \times 10^{-4}$) is much lower than that in Run 1. Figure 5 shows the outcome of Run 2. Growth of planetesimals during the earliest stage proceeds in a similar fashion to Run 1, as we ignore turbulent torques on planetesimals in both Runs 1 and 2. Once the largest planetesimals reach ~ 1000 km in size, pebble accretion starts to become efficient. 1000 km-size planetesimals grow faster than Run 1 on average since the scale height of pebbles is smaller in Run 2 than that in Run 1. However, in Run 2, growth of massive embryos by pebble accretion is halted due to their gap opening even before they start runaway gas accretion. Pebbles accumulate at outer gap edges and formation of another massive embryos at the gap edges occurs quickly. Some of embryos start runaway gas accretion, but their growth rates are low due to the low global gas accretion rate. As a result of these processes, several embryos with $\sim 10M_{\oplus}$ form in 3 Myr. Unlike Run1, no gas giant planet forms.

The other important difference between Run 1 and Run 2 is that Run 2 has a large number of 1000 km-size planetesimals in the end while almost no 1000 km-size planetesimals exist in the end of Run 1. In Run 2, these large planetesimals form at the gap edges opened by massive embryos. Since the gap width normalized by the Hill radius of a gap-opening embryo is much larger in Run 2 than Run 1, orbits of planetesimals at gap edges are dynamically stable in Run 2. The relative velocities between planetesimals and pebbles are low at the gap edge, as both gas and pebbles rotate nearly at the local Keplerian velocity. Because of these reasons, even 100 km-size planetesimals can efficiently grow to 1000 km in size at the gap edges in Run 2. In Run 1, in contrast, 1000 km-size planetesimals form only near the snow line in the early stage.

4.3. Run 10

For Run 10, we adopt large initial planetesimals ($M_0 = 10^{25}$ g) and the planetesimal formation timescale 10 times longer ($\tau_{\text{plan1}} = 1000$ yr) than that for Run 1. In Run 10, pebble accretion is efficient immediately after formation of planetesimals. In the end of the run, three gas giant planets form. Since the planetesimal formation timescale is long, many pebbles are not converted into planetesimals during radial drift and end up accumulating at outer edges of gaps opened by massive embryos. Pebbles accumulating at gap edges are eventually converted into planetesimals. Although these planetesimal are mostly ejected from the system due to strong gravitational perturbations of nearby embryos, a massive embryo (with a mass of $4M_{\oplus}$) forms at the gap edge of the outer most gas capturing embryo at ~ 4 Myr. We performed additional simulations using the same parameters if two more ice giant planets form at the gap edge so that they may result in Uranus and Neptune

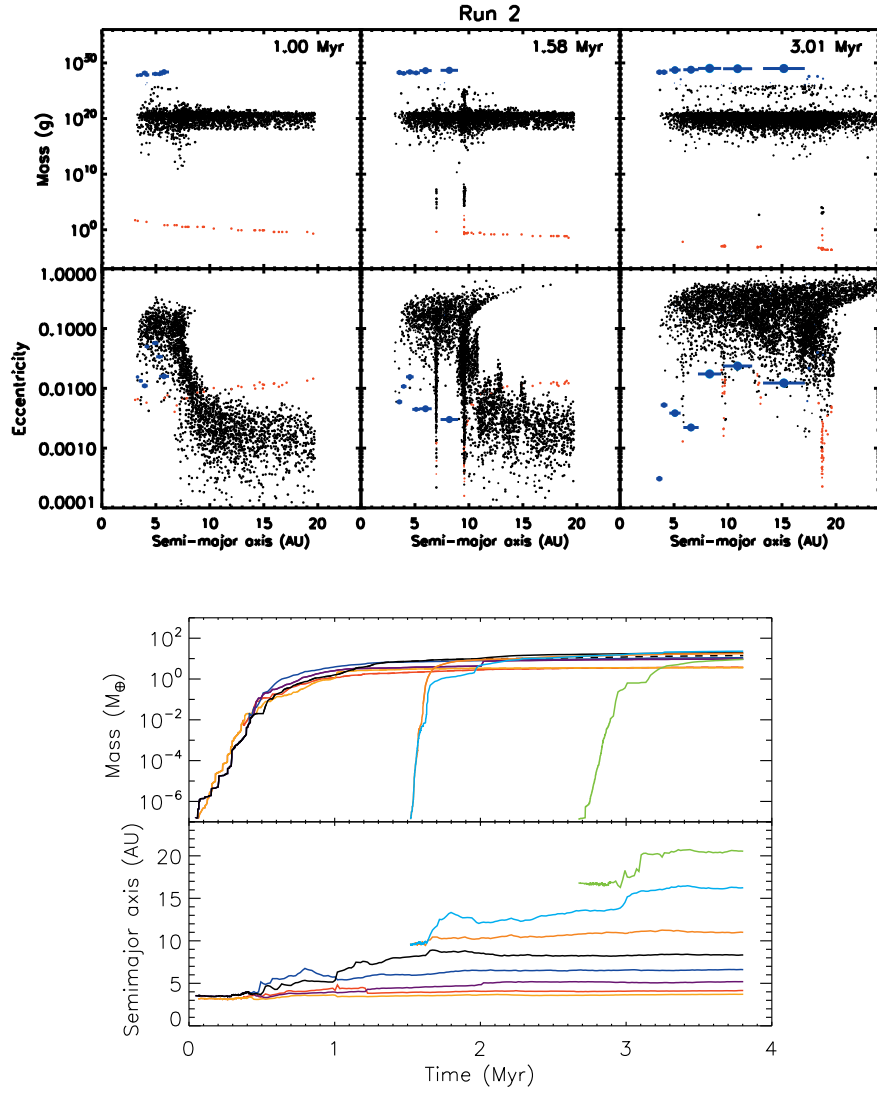


Figure 5: The same as Fig. 4 but for Run 2.

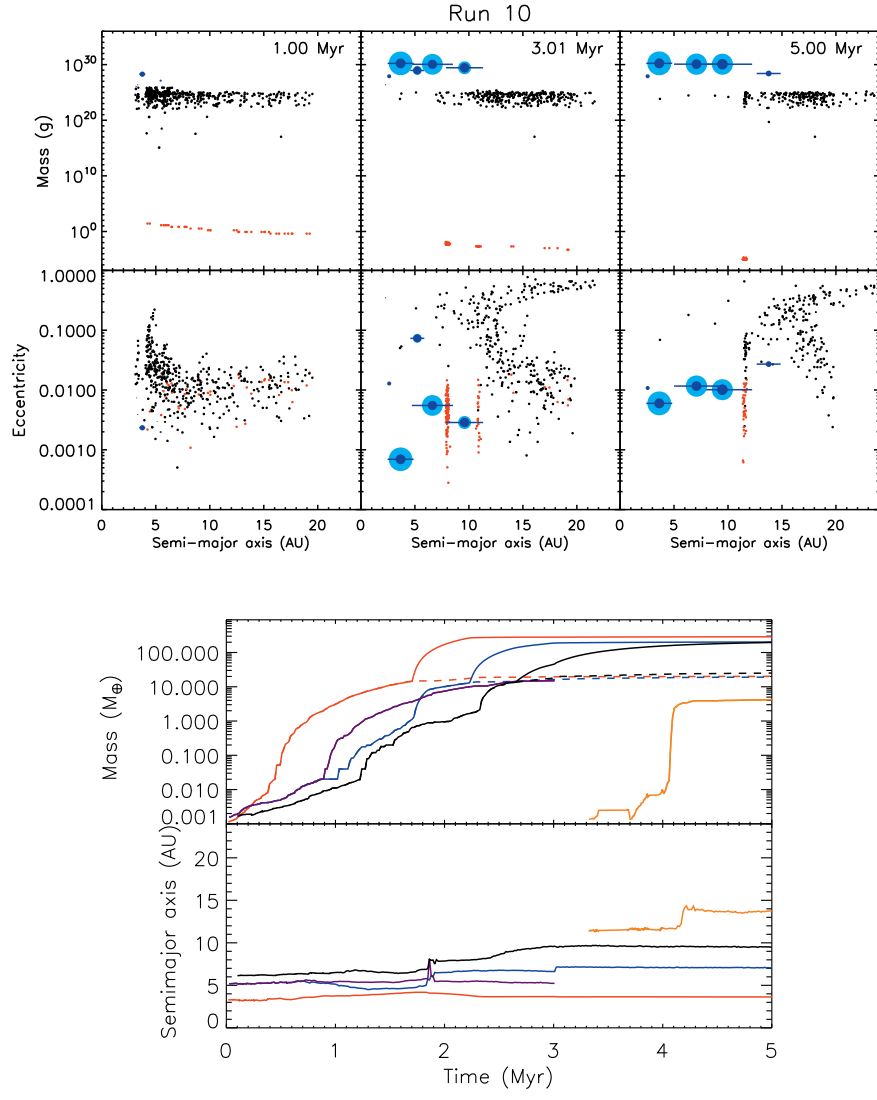


Figure 6: The same as Fig. 4 but for Run 10.

analogs. We found that formation two or more massive embryos at the same gap edge can occur but they end up merging into a single embryo in most cases.

Growth of embryos' cores after they start runaway gas accretion is much less than that in Run1, since the population of planetesimals is much lower in Run 10 than that in Run 1. The mass distribution of remaining planetesimals at > 10 AU is almost the same as the original size distribution, like Run 1.

5. Parameter dependence

In this section, we discuss how architectures of planetary systems depend on input parameters. Figure 7 shows architectures of planetary systems at 3 Myr for all the runs. Figure 8 shows the mass of the largest embryo as a function of key input parameters, α , M_0 , and St .

5.1. Reproducibility

We first discuss reproducibility for runs with the same input parameters. Since the statistical routine of our simulation code uses random numbers in several places, results cannot be the same even with the same initial conditions and the same input parameters. Run 1b and Run 1c have the same input parameters as Run 1. The numbers of gas giant planets and the masses of the largest gas giant planets are similar to each other for all the three runs. On the other hand, locations of small embryos are different; In Run 1b and Run 1c, there are no ice giant analogues outside the outermost gas giant planet, unlike Run 1 and our solar system.

This difference is found to be caused by stochasticity of planetesimal-driven migration of massive embryos. In Run 1, the largest embryo forms first near the snow line and embryos of ice giant analogues form later at slightly outer regions (> 5 AU). In Run 1b and Run 1c, on the other hand, a large embryo migrates outward and stays around 7 AU, stirring planetesimals there and preventing later formation of embryos there.

5.2. Turbulent viscosity

The effect of the turbulent viscosity has been already discussed in Section 4.2. As α increases, the mass of the largest embryo increases (the top panel of Fig. 8). This is because we adopt a gas surface density independent of α (Eq. (1)) and the global gas accretion rate is simply proportional to α . The locations of the largest embryos are generally at 7 – 10 AU regardless of α . The timescale of planetary accretion is too long for formation of massive gas giant planets beyond ~ 10 AU.

5.3. Initial planetesimal mass

Run 6 adopts very small initial planetesimals, $M_0 = 10^{13}$ g. This run has only one planet inside the snow line in the end. Pebbles at the gap edge push the gap opening embryo toward the central star. In most of runs, however, their total mass is usually much less than the embryo's mass, as pebbles are converted into planetesimals and they are subsequently ejected by the embryo. If planetesimals are small enough like the case of Run 6, they cannot

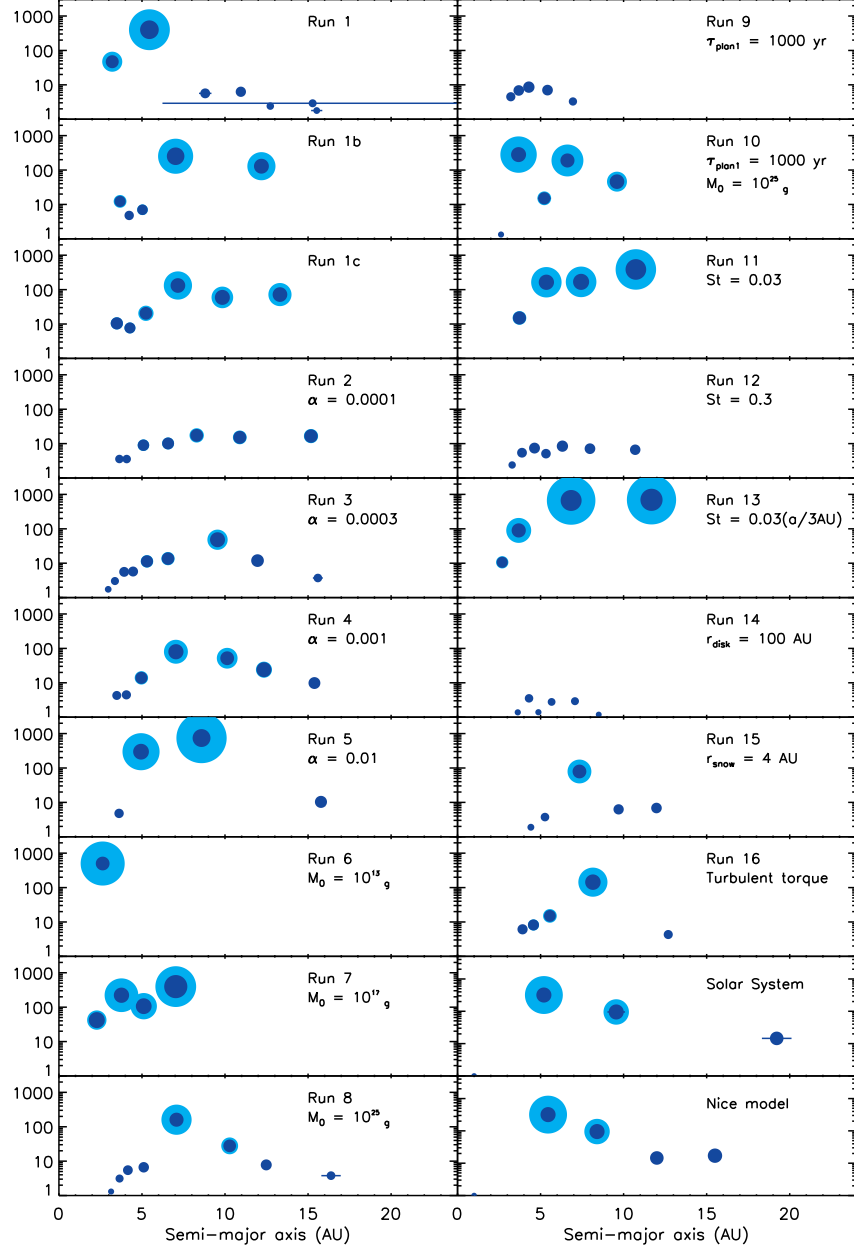


Figure 7: Orbital distribution of embryos at 3 Myr for all runs. Only massive embryos ($M > M_{\oplus}$) are shown. For reference, the Solar System and the initial condition of the Nice model (Tsiganis et al., 2005) are also shown. For Run 2 through Run 16, the parameters values that are different from Run 1 are shown on the top right of each panel. The horizontal bar for each body shows orbital excursion due to a finite orbital eccentricity.

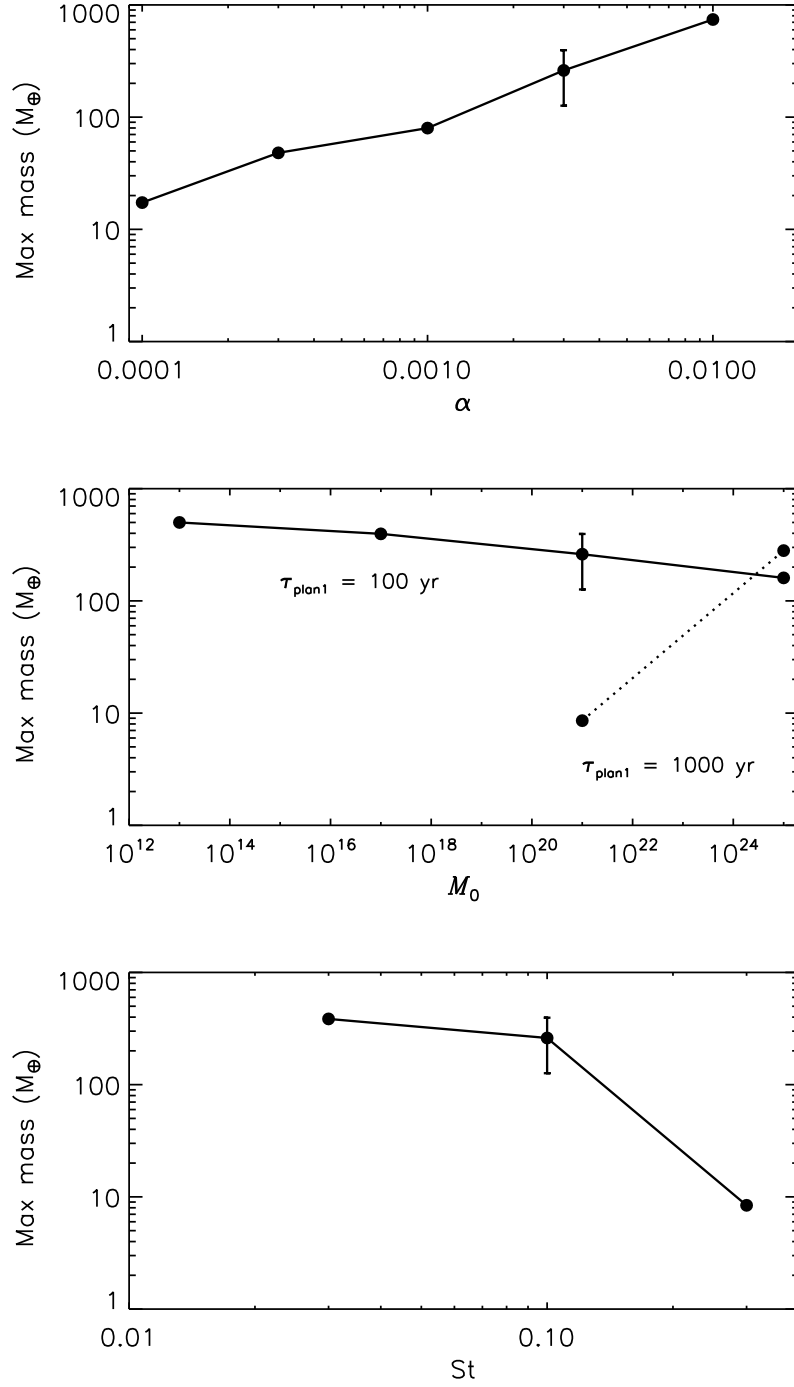


Figure 8: The mass of the most massive embryo at 3 Myr as a function of (top) α , (middle) M_0 , and (bottom) St . For the case with the base-line input parameters, we use the mean value and the standard deviation for Runs 1, 1b, and 1c.

be ejected as gas drag on small planetesimals are strong. Small planetesimals are quickly pulverized through collisional destruction to pebble-size fragments. Thus, the total amount of pebbles trapped at the gap edge increases with time and start to push the embryo very strongly. Since we assume that all pebbles sublimate at the snow line, the inward migration of the embryo stops at slightly inside the snow line.

For $\tau_{\text{plan1}} = 100$ yr, the mass of the most massive embryo decreases with increasing M_0 but only weakly (the middle panel of Fig. 8). For $\tau_{\text{plan1}} = 1000$ yr, gas giant planets form only for the case of $M_0 = 10^{25}$ g. Initially small planetesimals ($M_0 \leq 10^{21}$ g) grow very slowly if the population of planetesimals is small. For $M_0 = 10^{25}$ g, the maximum mass of the largest embryo is larger for longer τ_{plan1} . This is because the less frequently pebbles are converted into planetesimals, the larger the pebble flux to the largest embryo.

5.4. Pebble Stokes number (or size)

The mass of the largest embryo decreases with increasing St (the bottom panel of Fig. 8). For the case of $\text{St} = 0.3$, only several ice giant planets form without any gas giant planet. The dependence of the largest body's mass on St is caused by two reasons. First, efficient pebble accretion can occur for smaller planetesimals for smaller St . The transition from the hyperbolic regime to the settlement regime occurs if $\text{St} < \text{St}^* \propto M$ (Ormel and Klahr, 2010), where St^* is the critical St number. Second, the pebble accretion timescale for massive embryos is shorter for smaller St . For the 2D case ($R_{\text{coll}} \geq h_{\text{pe}}$), the pebble accretion rate \dot{M} is proportional to $\text{St}^{-1/3}$ for a given pebble flux (Morbidelli et al., 2015), while it is proportional to $\text{St}^{1/2}$ for the 3D case ($R_{\text{coll}} < h_{\text{pe}}$). Since the growth timescale is longer for massive embryos in the 2D regime than for small embryos in 3D regime (see Fig. 2), the overall timescale for a 1000 km-size planetesimal to grow to a massive embryo through both the regimes is shorter for smaller St .

We adopt constant pebble size for Run 13 instead of constant St for all other runs. The value of St at the snow line for Run 13 is 0.03, or the same as that for Run 11. We find similar masses of the largest bodies for these two runs. This implies that an important parameter is St around the snow line rather than the radial dependence of St .

5.5. Other parameters

The disk size is 100 AU for Run 14 while it is 200 AU for all other runs. The most massive planet produced in Run 14 is only $\sim 3M_{\oplus}$, since the pebble flux quickly ceases for small disks. Whether a protoplanetary disk is large or not is highly likely one of the most essential criteria for formation of gas giant planets.

The location of the snow line is 4 AU for Run 15 while it is 3 AU for all other runs. The mass of the largest embryo is smaller in Run 15 than Run 1. This is because the growth timescale of planetesimals due to mutual collisions increases with distance. If $M_0 = 10^{25}$ g, the effect of snow line location is probably relatively less important since the radial dependence of growth timescale by pebble accretion is relatively weaker than that by mutual collisions.

As shown by the snapshot of Run 16, the mass of the largest embryos becomes smaller with turbulent torques than that without the torques. Turbulent torques excite velocity

dispersion of planetesimals and slow down their growth. The effect of turbulent torques is insignificant for massive planetesimals or embryos.

6. Discussion and future work

One of our findings is that gas giant planets form in disks with a high viscous parameter α while systems with super-Earth- to Neptune-size planets tend to form in disks with a low α . On the other hand, Chambers (2016) found that gas giant planets tend to form in disks with a low α and that super-Earth-size planets do not form in his simulations, except in the presence of gas giant planets. The primal reason causing the different outcomes is different types of disk models applied in our and his simulations. While we adopted the same surface density profile independent of α provided that the disk surface density evolves in a non-viscous fashion, Chambers (2016) adopted purely viscously evolving disks using the analytic prescription of Chambers (2009). The disk accretion rate is proportional to α in our model while it remains moderately high even for a low α in a viscously evolving disk due to a high surface density. Matsumura et al. (2017) adopted the disk accretion rate fitted to the observational data (Hartmann et al. 1998) independent of α in their simulations. Thus, the disk surface density increases with decreasing α in their model, and the basic trend of their outcomes is similar to that seen in Chambers (2016).

It is difficult to conclude which disk models are more appropriate than others at this moment even though our understanding of protoplanetary disks rapidly advances, particularly owing to recent disk observations by the Atacama Large Millimeter Array (ALMA). The key parameter to understand angular momentum transport mechanisms of protoplanetary disks is the relationship between the disk mass and the disk accretion rate. Rafikov (2017) found no substantial correlation between the disk mass and the disk accretion rate for 26 samples resolved by ALMA (Ansdell et al., 2016) and that α varies from 10^{-4} to 0.04. One of his interpretations is that α is controlled by some yet uncertain mechanisms while the disk surface density evolves in a non-viscous manner, somewhat similar to the disk model we assumed. However, he also suggested other possibilities such as decoupling the global disk accretion rate at large distances from the central star and the gas accretion rate to the central star. Moreover, other authors claim some levels of correlation between the disk mass and the disk accretion rate (Manara et al., 2016; Lodato et al., 2017; Mulders et al., 2017), and classical viscous models can be still compatible with observations. Since the disk mass is often estimated from the dust abundance assuming the interstellar gas-dust ratio, direct measurements of gas densities probably help constrain which disk models are appropriate. Particularly, measurements of HD abundances (Bergin et al., 2013; McClure et al., 2016) in addition to CO abundance measurements are necessary to narrow down uncertainties of observed gas densities.

One of uncertain but intriguing parameters is the initial mass of the largest planetesimal M_0 . For the Solar System, it is probably possible to constrain M_0 by comparing the size distribution of remaining planetesimals with that for Kuiper belt objects. The mass distribution per logarithmic size for Kuiper belt has a peak at ~ 100 km in size (Fraser et al., 2014; Adams et al., 2014), potentially implying that this is the initial size of planetesimals

(Morbidelli et al., 2009). However, the mass distribution for Kuiper belt has another peak at the Pluto-size, ~ 3000 km, as the Pluto-size objects contain 10-50 % mass of the Kuiper belt (Nesvorný et al., 2017). If $M_0 = 10^{21}$ g (100 km-size planetesimals), pebble accretion produces a very steep size distribution above 100 km (Johansen et al., 2015), or too small a mass fraction of Pluto-size objects, although the steep slope is consistent with the slope for Kuiper belt objects between 100 km and ~ 300 km. Similar results are seen in most of our runs with $M_0 = 10^{21}$ g. Run 2, in which we adopted a very low turbulent viscosity, exceptionally showed a non-negligible population ($\sim 5\%$) of the Pluto-size objects, which form at the edges of gaps opened by massive embryos. Unfortunately, massive embryos quickly form at gap edges and their gravitational perturbations make orbits of Pluto-size objects highly eccentric, unlike nearly circular orbits seen in the initial state of the Nice model (Tsiganis et al., 2005). Our study implies that the Pluto-size objects in the Solar System are unlikely to have formed from 100 km-size objects through pebble accretion. There might have been two distinctive planetesimal formation mechanisms each of which produces 100 km-size and 3000 km-size planetesimals in the outer Solar System.

We assumed in this study that all pebbles are icy so that they quickly sublime inside the snow line. It is likely, however, that rocky pebbles exist inside the snow line, as evidenced by chondrules in chondritic meteorites. These pebbles are expected to be much smaller than icy pebbles due to inefficient mutual sticking. If it is the case, planetary growth by pebble accretion inside the snow line is inefficient due to a large scale height of small pebbles (Morbidelli et al., 2015). It is of interest to examine if dichotomy of planetary growth across the snow line is seen in simulations using our code. It is computationally demanding, however, for our code to handle small pebbles, as the time step for accurate orbital integration proportionally decreases with decreasing St .

Using molybdenum and tungsten isotope measurements on iron meteorites, Kruijer et al. (2017) demonstrated that meteorites were derived from two genetically distinct nebular reservoirs spatially separated at ~ 1 My after Solar System formation. They suggested that the separation was possibly caused by gap opening of proto-Jupiter. Such early formation of Jupiter might be difficult to reconcile with chondrule formation ages ranging over a few Myr (Amelin et al., 2002; Connelly et al., 2012), since chondrule-size pebbles are expected to quickly deplete inside the gap in the absence of pebble supply from the outer part of the disk. This problem might be resolved if the radial structure of the proto-solar nebula was very different from those assumed by standard models including the one adopted in this study. For example, the proto-solar nebula might have the inner cavity inside the asteroid belt so that chondrule-size pebbles piled up at the outer edge of the cavity.

7. Conclusion

In the present paper, we performed numerical simulations for formation of planetary systems taking into account pebble accretion. We varied the size of a protoplanetary disk, the turbulent viscosity, the pebble size, the planetesimal formation efficiency, and the initial mass distribution of planetesimals. If the planetesimal size exceeds 1000 km, pebble accretion becomes dominant for planetary growth than by planetesimal accretion. If the initial

planetesimal size is 100 km, the formation efficiency of planetesimals from pebbles need to be high to quickly form 1000 km-size planetesimals. Our simulations suggest that planetary systems like ours form from protoplanetary disks with moderately high turbulent viscosities. If the disk turbulent viscosity is low enough, a planet opens up a gap in the gaseous disk and halts accretion of pebbles even before the onset of runaway gas accretion. Formation of new planets at the gap edges is very efficient for cases of low turbulent viscosities. Such a disk produces a planetary system with several Neptune-size planets. The size distribution of remaining planetesimals is almost the same as the initial size distribution, except for the case of very low α . This low- α case showed formation of a non-negligible population of the Pluto-size objects for the initial planetesimal size of ~ 100 km, although most of the Pluto-size objects are highly eccentric unlike the initial condition suggested by the Nice model. There might have been two distinctive planetesimal formation mechanisms each of which produces 100 km-size and 3000 km-size planetesimals in the Kuiper belt.

Acknowledgements

This research was carried out in part at the Jet Propulsion Laboratory, California Institute of Technology, under contract with NASA. Government sponsorship acknowledged. Simulations were performed using a JPL supercomputer, Aurora.

Data sets

The source code is available at <https://github.com/rmorishima/PBHYB>.

Appendices

Appendix A: Gas drag coefficient C_D

We adopt the numerical coefficient C_D of Adachi et al. (1976) that covers all the ranges of the Mach number M_c and the Knudsen number K_n . The Mac and Knudsen numbers M_c and K_n are given as

$$M_c = \frac{v_{\text{rel}}}{\gamma^{1/2}c}, \quad K_n = \frac{\ell}{R}, \quad (27)$$

where v_{rel} is the relative velocity between the particle and ambient gas, $\gamma = 1.4$ is the heat capacity ratio, c is the isothermal sound speed, ℓ is the mean free path of gas molecule, and R is the particle radius. Using M_c and K_n , the Reynolds number, Re , is given as

$$\text{Re} = \frac{6Rv_{\text{rel}}}{c_m\ell} = \left(\frac{9\pi\gamma}{2}\right)^{1/2} \frac{K_n}{M_c}, \quad (28)$$

where $c_m (= (8/\pi)^{1/2}c)$ is the thermal velocity of gas.

For $M_c \ll 1$ and $K_n < 1$, we use the approximated formula given by Weidenschilling (1977) as

$$C_{D,\text{Wei}} = \begin{cases} 24\text{Re}^{-1} & (\text{for } \text{Re} < 1), \\ 24\text{Re}^{-0.6} & (\text{for } 1 \leq \text{Re} < 800), \\ 0.44 & (\text{for } \text{Re} \geq 800), \end{cases} \quad (29)$$

where the case of $\text{Re} < 1$ is in the Stokes drag regime. For $M_c \ll 1$ and $K_n > 1$, the gas drag is in the Epstein drag regime as

$$C_{D,\text{Eps}} = \frac{8c_m}{3v_{\text{rel}}}. \quad (30)$$

We give the drag coefficient $C_{D,\text{low}}$ for $M_c \ll 1$ as

$$C_{D,\text{low}} = \text{Min}(C_{D,\text{Wei}}, C_{D,\text{Eps}}). \quad (31)$$

Finally, we interpolate the drag coefficient over M_c as (Brasser et al., 2007)

$$C_D = \begin{cases} C_{D,\text{high}}M_c^2 + C_{D,\text{low}}(1 - M_c^2) & (\text{for } M_c \leq 1), \\ C_{D,\text{high}} & (\text{for } M_c > 1), \end{cases} \quad (32)$$

where $C_{D,\text{high}} = 2$.

Appendix B: Turbulent torques

Okuzumi and Ormel (2013) derived the stirring rates of planetesimals in turbulence driven by magneto-rotational instability (MRI). The diffusion coefficient D_a of the semi-major axis a of a body for the ideal MHD case is

$$D_a = 0.55 \left(\frac{\Sigma_{\text{gas}} a^2}{M_*} \right)^2 \alpha a^2 \Omega, \quad (33)$$

where Σ_{gas} is the gas surface density, M_* is the mass of the central star, α is the viscosity parameter, and Ω is the Keplerian frequency at a . At the low eccentricity limit, the change δa of a during a time step δt is given as $\delta a = f_{\text{den},\theta} \delta t (2/\Omega)$, where $f_{\text{den},\theta}$ is the tangential force due to density fluctuation. Since $D_a = (1/2)(\langle(\delta a)^2\rangle/\delta t)$, we give $f_{\text{den},\theta}$ as

$$f_{\text{den},\theta} = \frac{\Omega}{2} \xi \left(\frac{2D_a}{\delta t} \right)^{1/2}, \quad (34)$$

where ξ is the Gaussian white noise with a standard deviation of unity. We give the forces in the radial (r) and vertical (z) directions in a similar manner, assuming isotropic turbulence as is the case of aerodynamic turbulent drag.

Appendix C: Collision probability for the statistical routine

The expected change rate of the mass M of a planetesimal in the target tracer due to merging with planetesimals or pebbles in the interloping tracer j is given by (Morishima, 2015)

$$\left(\frac{dM}{dt} \right)_j = n_j M_j a_{ij}^2 h_{ij}^2 \Omega P_{\text{col}}, \quad (35)$$

where n_j is the surface number density of planetesimals/pebbles in the tracer j , M_j is the mass of a constituent planetesimal/pebble, a_{ij} is the mean semimajor axis of the target and the interloper, h_{ij} is the reduced mutual Hill radius of the target and interloper, and P_{col} is the non-dimensional collision probability (see Morishima (2015) for more details). The Hill radius R_{Hill} is given by $a_{ij} h_{ij}$. In the statistical routine adopted for the study of the present paper, the target is always a planetesimal-tracer, as we do not explicitly handle collisions between pebbles. As described in the main text, planetesimals are defined as bodies with Stokes number larger than 2. Smaller particles are called pebbles. Different prescriptions are used for pebble and planetesimal interlopers.

C.1. Planetesimal-interlopers

If the interloper is a planetesimal-tracer ($\text{St} > 2$) its orbit is well approximated by a Keplerian orbit. Thus, we calculate the collision probability P_{col} as done in Morishima (2015). We call this probability $P_{\text{col,M15}}$ to distinguish from others described below. This probability corresponds to that for the hyperbolic regime in Ormel and Klahr (2010).

Ormel and Klahr (2010) showed that even for $\text{St} > 2$, due to three body capture, the collision probability becomes significantly larger than that for the hyperbolic regime if both St and the relative velocity are low enough. Ormel and Kobayashi (2012) derived an empirical form of the collisional radius b_{3b} normalized by the Hill radius for this effect as

$$b_{3b} = \frac{1}{\text{St}} \exp \left[- \left(\frac{0.7 \tilde{v}_r}{\text{St}} \right)^5 \right], \quad (36)$$

where \tilde{v}_r is the non-dimensional relative velocity. We give the relative velocity as

$$\tilde{v}_r = \sqrt{\tilde{e}_{ij}^2 + \tilde{i}_{ij}^2}, \quad (37)$$

where \tilde{e}_{ij} and \tilde{i}_{ij} are the relative eccentricity and inclination normalized by h_{ij} . Using b_{3b} , the collision probability $P_{\text{col},3b}$ is given by the smaller of the 3D or the 2D collision probability as

$$P_{\text{col},3b} = \text{MIN}(\pi b_{3b}^2 \tilde{v}_r / \tilde{i}_{ij}, 2b_{3b} \tilde{v}_r). \quad (38)$$

The collision probability P_{col} for $\text{St} > 2$ is given by

$$P_{\text{col}}(\text{St} > 2) = \text{MAX}(P_{\text{col},\text{M15}}, P_{\text{col},3b}). \quad (39)$$

If the interloper merges with the target, the velocity of the target is updated in the same manner of Morishima (2015).

C. 2. Pebble-interlopers

If the interloper is a pebble-tracer ($\text{St} \leq 2$), the accretion modes are divided into two regimes depending on the relative velocity. The threshold relative speed that separates these two regimes is represented by the critical Stokes number St_{crit} , which is given as (Ormel and Klahr, 2010)

$$\text{St}_{\text{crit}} = \text{MIN} \left[\frac{12}{\tilde{v}_r^3}, 2 \right]. \quad (40)$$

If $\text{St} \leq \text{St}_{\text{crit}}$ or in the settlement regime, pebbles settle toward a large body during close encounters with the target. The non-dimensional collisional radius in this regime is given as (Ormel and Kobayashi, 2012)

$$b_{\text{set}} = \text{MIN} \left[\left(\frac{12\text{St}}{\tilde{v}_r} \right)^{1/2}, 2\text{St}^{1/3} \right] \times \exp \left[- \left(\frac{\text{St}}{\text{St}_{\text{crit}}} \right)^{0.65} \right]. \quad (41)$$

It is inappropriate to use instantaneous Keplerian elements for evaluation of the relative velocity between a pebble-tracer and a target. We evaluate the relative velocity in a different manner than that for $\text{St} > 2$ as follows. The velocity vector and the radial position of the target are given by \mathbf{v} and r , and those for the interloper are given by the same symbols but with the index of j . For each particle, its velocity relative to the local Keplerian velocity $\mathbf{v}_{\text{kep}}(r)$ for a body with a circular and non-inclined orbit is calculated as

$$\mathbf{v}' = \mathbf{v} - \mathbf{v}_{\text{kep}}(r), \quad (42)$$

$$\mathbf{v}'_j = (\mathbf{v}_j - \mathbf{v}_{\text{kep}}(r_j)) \left(\frac{r_j}{r} \right)^{1/2}, \quad (43)$$

where the factor $(r_j/r)^{1/2}$ adjusts the local velocity difference at r and r_j . Using the relative velocity components in the cylindrical coordinates, the non-dimensional relative speed between the target and the interloper is the given as

$$\tilde{v}_r = \frac{[(v'_r - v'_{j,r})^2 + (v'_\theta - v'_{j,\theta})^2 + (v'_z - v'_{j,z})^2]^{1/2}}{a_{ij} h_{ij} \Omega}. \quad (44)$$

If $\text{St} \geq \text{St}_{\text{crit}}$ or in the hyperbolic regime, the non-dimensional collisional radius is given as

$$b_{\text{hyp}} = \tilde{r}_{\text{p}} \sqrt{1 + \frac{6}{\tilde{r}_{\text{p}} \tilde{v}_{\text{r}}^2}}, \quad (45)$$

where $\tilde{r}_{\text{p}} = (s + s_j)/(a_{ij} h_{ij})$ is the non-dimensional physical radius with the physical radius of a constituent body in the target s and that in the interloper s_j .

The non-dimensional collisional radius for $\text{St} \leq 2$ is given by the larger of those in the settlement and hyperbolic regimes as

$$b_{\text{col}}(\text{St} \leq 2) = \text{MAX}[b_{\text{set}}, b_{\text{hyp}}]. \quad (46)$$

The collision probability for $\text{St} \leq 2$ is given as

$$P_{\text{col}}(\text{St} \leq 2) = \text{MIN} \left[2b_{\text{col}} \tilde{v}_{\text{r}}, \frac{\pi b_{\text{col}}^2 \tilde{v}_{\text{r}}}{\sqrt{2\pi} h_{\text{peb}}} \exp \left(-\frac{z_i^2}{2h_{\text{peb}}^2} \right) \right], \quad (47)$$

where h_{peb} is the scale height of pebbles (see the caption of Fig. 1 for the exact form of h_{peb}).

If the interloper is merged with the target, the velocity of the target relative to the local Keplerian velocity is updated by summing up the momenta in the cylindrical coordinates as

$$\mathbf{v}'_{i,\text{new}} = \frac{[(Mv'_{i,r} + \Delta Mv'_{j,r}), (Mv'_{i,\theta} + \Delta Mv'_{j,\theta}), (Mv'_{i,z} + \Delta Mv'_{j,z})]}{M + \Delta M}, \quad (48)$$

where ΔM is the mass increase of the target planetesimal (Eq. (13) of Morishima (2015)).

Appendix D: Capture of planetesimals/pebbles in embryo atmospheres

Ormel and Kobayashi (2012) derived the approximate analytic solution of the structure of a planetary atmosphere, provided that heat transport is taken place by radiation only. The atmosphere density ρ_{atm} relative to the local nebula density ρ_{gas} is defined as $\sigma = \rho_{\text{atm}}/\rho_{\text{gas}}$. The non-dimensional density σ as a function of distance x from the planetary center is given as

$$\frac{s_{\text{Bond}}}{x} = \begin{cases} 1 + \frac{2W_{\text{neb}}(\sigma - 1) + \ln \sigma}{\gamma} & (\text{for } \sigma < \sigma_{\text{t}}), \\ \frac{s_{\text{Bond}}}{x_{\text{t}}} + \frac{4}{\gamma}(4W_{\text{neb}})^{1/3} (\sigma^{1/3} - \sigma_{\text{t}}^{1/3}) & (\text{for } \sigma \geq \sigma_{\text{t}}), \end{cases} \quad (49)$$

where W_{neb} is the non-dimensional parameter

$$W_{\text{neb}} = \frac{3\kappa L P_{\text{gas}}}{64\pi\sigma_{\text{SB}} G M T_{\text{gas}}^4}, \quad (50)$$

and L is the luminosity of the planetary atmosphere

$$L = \frac{GM\dot{M}}{R}. \quad (51)$$

Here $s_{\text{Bond}} = GM/c^2$ is the atmospheric Bondi radius, κ is the atmospheric opacity, P_{gas} and T_{gas} are the pressure and the temperature of the local nebula, and σ_{SB} is the Stefan-Boltzmann constant.

The density σ_t at the transition between the nearly isothermal outer region and the warmer inner region is given as

$$\sigma_t = \frac{0.2}{W_{\text{neb}}}, \quad (52)$$

and the transition radius x_t is given by inserting σ_t into Eq. (49). The critical atmospheric density for capturing a body with radius s_j is (Inaba and Ikoma, 2003)

$$\rho_c = \frac{2}{3} \left(\frac{v_\infty^2}{2GM} + \frac{1}{R_H} \right) s_j \rho_p, \quad (53)$$

where v_∞ is the relative velocity at infinity. In our code, v_∞ is approximately evaluated when the separation x is $4.5R_H$ during orbital integration. The capture radius $s_{\text{atm}} = x(\rho_c)$ is given by setting $\sigma = \rho_c/\rho_{\text{gas}}$ in Eq. (49). If $s_{\text{atm}} > s$, s is replaced by s_{atm} in the calculation of P_{col} . We assume that s_{atm} exceeds neither s_{Bond} nor $0.25R_H$ (Lissauer et al., 2009).

The atmospheric mass is assumed to be much less than the mass of the solid core for the derivation of the above analytic atmospheric structure. This is not correct if the embryo is massive enough to trigger runaway gas accretion. Atmospheric models for massive embryos using realistic equation states show that the most of atmospheric mass is concentrated near the solid core (Lee and Chiang, 2015). Therefore, it is expected that the structure of the less massive outer part of the atmosphere is still approximately given by the above analytic formulation, if the core mass is replaced by the total mass of the core and atmosphere. We adopt this assumption for embryos in runaway gas accretion in the present study.

Appendix E: Collisional destruction

Collisional outcome depends on the specific impact energy Q and the specific energy required to disperse half of the mass of the target Q_D^* . The energy Q is given as

$$Q = \frac{1}{2} \frac{MM_j v_{\text{imp}}^2}{(M + M_j)^2}, \quad (54)$$

where M_j is the mass of the impactor and v_{imp} is the impact velocity. We adopt Q_D^* modeled by Benz and Asphaug (1999) as

$$Q_D^* = Q_0 \left(\frac{s}{1 \text{ cm}} \right)^j + B \rho_p \left(\frac{s}{1 \text{ cm}} \right)^k, \quad (55)$$

where s is the target radius, Q_0 , B , j , and k are the fitting parameters. We adopt the values for impacts on ice at $v_{\text{imp}} = 3 \text{ km s}^{-1}$ from Table III of Benz and Asphaug (1999).

We adopt the prescription of the size distribution of ejecta yielded from the impact following Kobayashi and Tanaka (2010). The prescription assumes that impact yields a

largest remnant body and a number of small fragments. The total mass of fragments M_{frag} is given as

$$M_{\text{frag}} = (M + M_j) \frac{\phi}{1 + \phi}, \quad (56)$$

where $\phi = Q/Q_D^*$. The mass of the largest remnant M_{lr} is given as

$$M_{\text{lr}} = M + M_j - M_{\text{frag}}. \quad (57)$$

The mass distribution of fragments follows $dn/dM \propto M^{-11/6}$ (Dohnanyi, 1969) and the mass of the largest fragment is

$$M_{\text{lf}} = \frac{0.2M_{\text{frag}}}{1 + \phi}. \quad (58)$$

We apply fragmentation or collisional erosion only to tracer-tracer collisions, not to embryos. The procedure to handle fragmentation in the code is as follows. We first merge the target and the impactor through the procedure described in Morishima (2015) (see also Appendix C). This gives the position and the velocity of the new tracer. We then simply replace the mass of a constituent planetesimal following the mass distribution described above and adjust the number of planetesimals in the tracer so the tracer's mass is unchanged. If a random number, which uniformly takes between 0 and 1, is lower than $M_{\text{lr}}/(M + M_j)$, the new planetesimal's mass is assigned to be M_{lr} . Otherwise, the new planetesimal's mass is a fragment's mass M given by $\text{rn} = (M/M_{\text{lf}})^{1/6}$, where rn is another random number between 0 and 1. If the Stokes number of the assigned fragment is lower than St for pebbles we set its mass so that its Stokes number is the pebble's St .

References

References

- Adachi, I., Hayashi, C., Nakazawa, K., 1976. The gas drag effect on the elliptical motion of a solid body in the primordial solar nebula. *Prog. Theoret. Phys.* 56, 1756–1771.
- Adams, E.R., Gulbis, A.A.S., Elliot, J.L., Benecchi, S.D., Buie, M.W., Trilling, D.E., Wasserman, L.H., 2014. De-biased populations of Kuiper belt objects from the deep ecliptic survey. *Astron. J.* 148, 55.
- Amelin, Y., Krot, A.N., Hutcheon, I.D., Ulyanov, A.A., 2002. Lead isotopic ages of chondrules and Calcium-Aluminium-Rich inclusions. *Science* 297, 1678–1683.
- Ansdell, M., et al., 2016. ALMA survey of Lupus protoplanetary disks. I. Dust and gas masses. *Astrophys. J.* 828, 46.
- Bai, X.N., 2013. Wind-driven accretion in protoplanetary disks. II. Radial dependence and global picture. *Astrophys. J.* 772, 96.
- Benz, W., Asphaug, E., 1999. Catastrophic disruption revisited. *Icarus* 142, 5–20.
- Bergin, E.A., et al., 2013. An old disk still capable of forming a planetary system. *Nature* 493, 644–646.
- Birnstiel, T., Dullemond, C.P., Brauer, F., 2010. Gas- and dust evolution in protoplanetary disks. *Astron. Astrophys.* 513, A79.
- Birnstiel, T., Klahr, H., Ercolano, B., 2012. A simple model for the evolution of the dust population in protoplanetary disks. *Astron. Astrophys.* 539, A148.
- Bitsch, B., Lambrechts, M., Johansen, A., 2015. The growth of planets by pebble accretion in evolving protoplanetary discs. *Astron. Astrophys.* 582, A112.
- Brasser, R., Duncan, M., Levison, H.F., 2007. Embedded starclusters and the formation of the Oort cloud II. The effect of the primordial solar nebula. *Icarus* 191, 413–433.
- Capobianco, C.C., Duncan, M.J., Levison, H.F., 2011. Planetesimal-driven planet migration in the presence of a gas disk. *Icarus* 211, 819–831.
- Carrera, D., Johansen, A., Davies, M.B., 2015. How to form planetesimals from mm-sized chondrules and chondrule aggregates. *Astron. Astrophys.* 579, A43.
- Chambers, J.E., 2009. An analytic model for the evolution of a viscous, irradiated disk. *Astrophys. J.* 705, 1206–1214.
- Chambers, J.E., 2014. Giant planet formation with pebble accretion. *Icarus* 233, 83–100.
- Chambers, J.E., 2016. Pebble accretion and diversity of planetary systems. *Astrophys. J.* 825, 63.
- Connelly, J.N., Bizzarro, M., Krot, A.N., Nordlund, Å., Wielandt, D., Ivanova, M.A., 2012. The absolute chronology and thermal processing of solids in the solar protoplanetary disk. *Science* 338, 651–655.
- Dohnanyi, J.S., 1969. Collisional model of asteroids and their debris. *J. Geophys. Res.* 74, 2351–2554.
- Dubrulle, R., Morfill, G., Sterzik, M., 1995. The dust subdisk in the protoplanetary nebula. *Icarus* 114, 237–246.
- Duffell, P.C., 2015. A simple analytic model for gaps in protoplanetary disks. *Astrophys. J. Lett.* 807, L11.
- Fraser, W.C., Brown, M.E., Morbidelli, A., Parker, A., Batygin, K., 2014. The absolute magnitude distribution function of Kuiper belt objects. *Astrophys. J.* 782, 100.
- Genda, H., Kokubo, E., Ida, S., 2012. Merging criteria for giant impacts of protoplanets. *Astrophys. J.* 744, 137.
- Goodman, J., Rafikov, R.R., 2001. Planetary torques as the viscosity of protoplanetary disks. *Astrophys. J.* 552, 793–802.
- Hayashi, C., 1981. Structure of the solar nebula, growth and decay of magnetic fields and effects of magnetic and turbulent viscosities on the nebula. *Suppl. Prog. Theoret. Phys.* 70, 35–53.
- Ida, S., Guillot, T., Morbidelli, A., 2008. Accretion and destruction of planetesimals in turbulent disks. *Astrophys. J.* 686, 1292–1301.
- Ida, S., Guillot, T., Morbidelli, A., 2016. The radial dependence of pebble accretion rates: a source of diversity in planetary systems I. Analytic formulation. *Astron. Astrophys.* 591, A72.
- Ikoma, M., Nakazawa, K., Emori, H., 2000. Formation of giant planets: Dependence on core accretion rate and grain opacity. *Astrophys. J.* 537, 1013–1025.

- Inaba, S., Ikoma, M., 2003. Enhanced collisional growth of a protoplanet that has an atmosphere. *Astron. Astrophys.* 410, 711–723.
- Inaba, S., Wetherill, G., Ikoma, M., 2003. Formation of gas giant planets: core accretion models with fragmentation and planetary envelope. *Icarus* 166, 46–62.
- Johansen, A., Mac Low, M.M., Lacerda, P., Bizzarro, M., 2015. Growth of asteroids, planetary embryos, and Kuiper belt objects by chondrule accretion. *Science Advances* 1, 1500109.
- Kanagawa, K.D., Tanaka, H., Muto, T., Tanigawa, T., 2017. Modelling of deep gaps created by giant planets in protoplanetary disks. *Publ. Astron. Soc. Jpn* 69, 97.
- Kobayashi, H., Tanaka, H., 2010. Fragmentation model dependence of collision cascades. *Icarus* 206, 735–746.
- Kobayashi, H., Tanaka, H., Krivov, A.V., 2011. Planetary core formation with collisional fragmentation and atmosphere to form gas giant planets. *Astrophys. J.* 738, 35.
- Krijt, S., Ormel, C.W., Dominik, C., Tielens, A.G.G.M., 2015. Erosion and the limits to planetesimal growth. *Astron. Astrophys.* 574, A83.
- Kruijer, T.S., Burkhardt, C., Budde, G., Kleine, T., 2017. Age of Jupiter inferred from the distinct genetics and formation times of meteorites. *Proc. Natl. Acad. Sci.* 114, 6712–6716.
- Lambrechts, M., Johansen, A., 2012. Rapid growth of giant-cores by pebble accretion. *Astron. Astrophys.* 544, A32.
- Lambrechts, M., Johansen, A., 2014a. Forming the cores of giant planets from the radial pebble flux in protoplanetary disks. *Astron. Astrophys.* 572, A107.
- Lambrechts, M., Johansen, A., 2014b. Separating gas-giant and ice-giant planets by halting pebble accretion. *Astron. Astrophys.* 572, A35.
- Laughlin, G., Steinacker, A., Adams, F.C., 2004. Type I planetary migration with MHD turbulence. *Astrophys. J.* 608, 489–496.
- Lee, E.J., Chiang, E., 2015. To cool is to accrete: Analytic scalings for nebular accretion of planetary atmospheres. *Astrophys. J.* 811, 41.
- Levison, H.F., Duncan, M.J., Thommes, E., 2012. A Lagrangian integrator for planetary accretion and dynamics. *Astrophys. J.* 144, 119.
- Levison, H.F., Kretke, K.A., Duncan, M.J., 2015. Growing the gas-giant planets by the gradual accumulation of pebbles. *Nature* 524, 322–324.
- Lissauer, J.J., Hubickyj, O., D’Angelo, G., Bodenheimer, P., 2009. Models of Jupiter’s growth incorporating thermal and hydrodynamic constraints. *Icarus* 199, 338–350.
- Lodato, G., Scardoni, C.E., Manara, C.F., Testi, L., 2017. Protoplanetary disc ‘isochrones’ and the evolution of discs in the \dot{M} – M_d plane. *Mon. Notice Royal Astron. Soc.* 472, 4700–4706.
- Lodders, K., 2010. Solar System abundances of the elements, in: Goswami, A., Reddy, B.E. (Eds.), *Principles and Perspectives in Cosmochemistry*, Springer-Verlag. p. 379.
- Lubow, S.H., D’Angelo, G., 2006. Gas flow across gaps in protoplanetary disks. *Astrophys. J.* 641, 526–533.
- Machida, R., Abe, Y., 2010. Terrestrial planet formation through accretion of sublimating icy planetesimals in a cold nebula. *Astrophys. J.* 716, 1252–1262.
- Manara, C.F., et al., 2016. Evidence for a correlation between mass accretion rates onto young stars and the mass of their protoplanetary disks. *Astron. Astrophys.* 591, L3.
- Matsumura, S., Brasser, R., Ida, S., 2017. *N*-body simulations of planet formation via pebble accretion. I. First results. *Astron. Astrophys.* 607, A67.
- McClure, M.K., et al., 2016. Mass measurements in protoplanetary disks from hydrogen deuteride. *Astrophys. J.* 831, 167.
- Morbidelli, A., Bottke, W.F., Nesvorný, D., Levison, H.F., 2009. Asteroids were born big. *Icarus* 204, 558–573.
- Morbidelli, A., Lambrechts, M., Jacobson, S., Bitsch, B., 2015. The great dichotomy of the Solar System: Small terrestrial embryos and massive giant planet cores. *Icarus* 258, 418–429.
- Morishima, R., 2015. A particle-based hybrid code for planet formation. *Icarus* 260, 368–395.
- Morishima, R., 2017. Onset of oligarchic growth and implication for accretion histories of dwarf planets.

- Icarus 281, 459–475.
- Morishima, R., Stadel, J., Moore, B., 2010. From planetesimals to terrestrial planets: N -body simulations including the effects of nebular gas and giant planets. *Icarus* 207, 517–535.
- Mulders, G.D., Pascucci, I., Manara, C.F., Testi, L., Herczeg, G.J., Henning, T., Mohanty, S., Lodato, G., 2017. Constraints from dust mass and mass accretion rate measurements on angular momentum transport in protoplanetary disks. *Astrophys. J.* 847, 31.
- Nakazawa, K., Ida, S., Nakagawa, Y., 1989. Collisional probability of planetesimals revolving in the solar gravitational field. I. Basic formulation. *Astron. Astrophys.* 220, 293–300.
- Nesvorný, D., Vokrouhlický, D., Dones, L., Levison, H.F., Kaib, N., Morbidelli, A., 2017. Origin and evolution of short-period comets. *Astron. J.* 845, 27.
- Ohsawa, R., Onaka, T., Yasui, C., 2015. Impact of the initial disk mass function on the disk fraction. *Publ. Astron. Soc. Jpn* 67, 1209.
- Okuzumi, S., Ormel, C.W., 2013. The fate of planetesimals in turbulent disks with dead zones. I. The turbulent stirring recipe. *Astrophys. J.* 771, 43.
- Okuzumi, S., Tanaka, H., Kobayashi, H., Wada, K., 2012. Rapid coagulation of porous dust aggregates outside the snow line: A pathway to successful icy planetesimal formation. *Astrophys. J.* 752, 106.
- Ormel, C.W., Cuzzi, J.N., 2007. Close-form expressions for particle relative velocities induced by turbulence. *Astron. Astrophys.* 466, 413–420.
- Ormel, C.W., Klahr, H.H., 2010. The effect of gas drag on the growth of protoplanets: Analytic expressions for the accretion of small bodies in laminar disks. *Astron. Astrophys.* 520, A43.
- Ormel, C.W., Kobayashi, H., 2012. Understanding how planets become massive. I. Description and validation of a new toy model. *Astrophys. J.* 747, 115.
- Owen, J.E., Clarke, C.J., Ercolano, B., 2012. On the theory of disc photoevaporation. *Mon. Notice Royal Astron. Soc.* 422, 1880–1901.
- Papaloizou, J.C.B., Larwood, J.D., 2000. On the orbital evolution and growth of protoplanets embedded in a gaseous disc. *Mon. Notice Royal Astron. Soc.* 315, 823–833.
- Pollack, J.B., Hubickyj, O., Bodenheimer, P., Jissauer, J.J., 1996. Formation of the giant planets concurrent accretion of solid and gas. *Icarus* 124, 62–85.
- Rafikov, R.R., 2017. Protoplanetary disks as (possibly) viscous disks. *Astrophys. J.* 837, 163.
- Sato, T., Okuzumi, S., Ida, S., 2016. On the water delivery to terrestrial embryos by ice pebble accretion. *Astron. Astrophys.* 589, A15.
- Schäfer, U., Yang, C.C., Johansen, A., 2017. Initial mass function of planetesimals formed by the streaming instability. *Astron. Astrophys.* 597, A69.
- Shakura, N.I., Sunyaev, R.A., 1973. Black holes in binary systems. Observational appearance. *Astron. Astrophys.* 24, 337–355.
- Simon, J.B., Armitage, P.J., Li, R., Youdin, A.N., 2016. The mass and size distribution of planetesimals formed by the streaming instability. I. The role of self-gravity. *Astrophys. J.* 822, 55.
- Stepinski, T.F., 1998. The solar nebula as a process – An analytic model. *Icarus* 132, 100–112.
- Suzuki, T., Inutsuka, S., 2014. Magnetohydrodynamic simulations of global accretion disks with vertical magnetic fields. *Astrophys. J.* 784, 121.
- Tanaka, H., Ward, W.R., 2004. Three-dimensional interaction between a planet and an isothermal gaseous disk. II. Eccentricity waves and bending waves. *Astrophys. J.* 602, 388–395.
- Tsiganis, K., Gomes, R., Morbidelli, A., Levison, H.F., 2005. Origin of the orbital architecture of the giant planets of the Solar System. *Nature* 435, 459–461.
- Weidenschilling, S.J., 1977. Aerodynamics of solid bodies in the solar nebula. *Mon. Notice Royal Astron. Soc.* 180, 57–70.
- Weidenschilling, S.J., 2011. Initial sizes of planetesimals and accretion of the asteroids. *Icarus* 214, 671–684.
- Wilson, J.D., Sawford, B.L., 1996. Review of Lagrangian stochastic models for trajectories in the turbulent atmosphere. *Bound.-Layer Meteorol.* 78, 191–210.